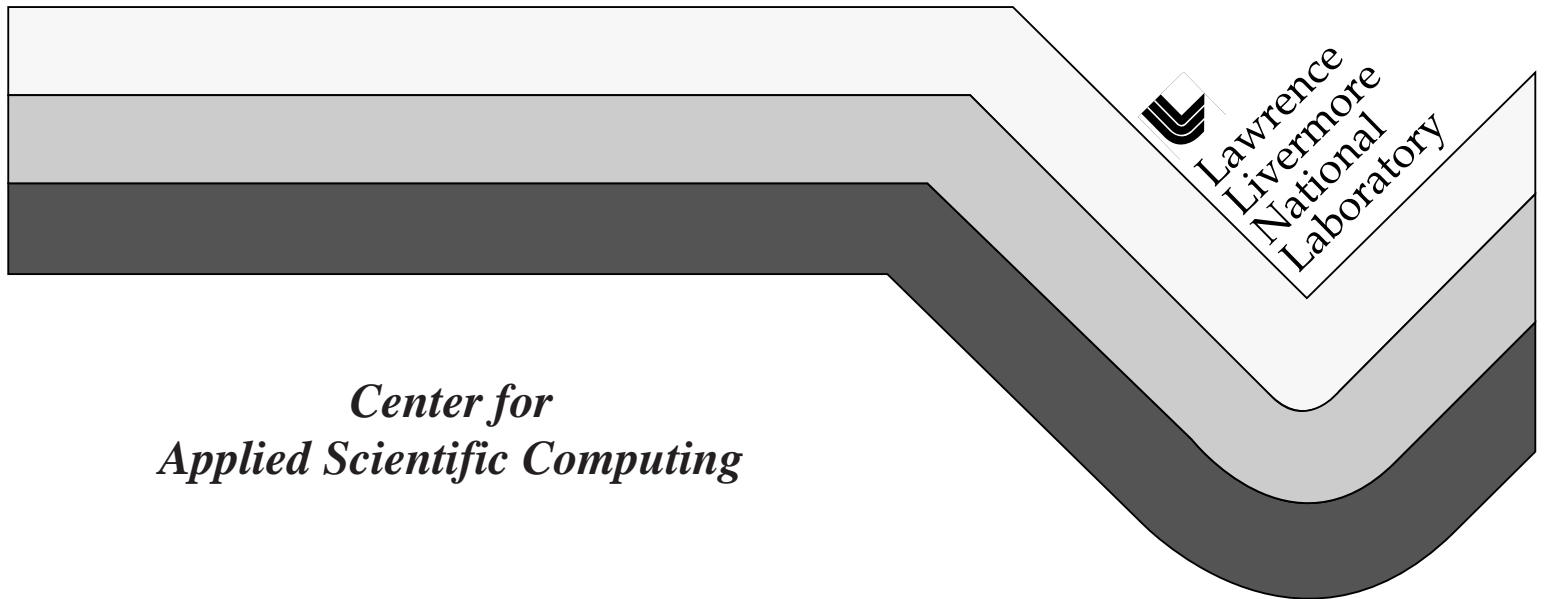


A Conservative Adaptive-Mesh Algorithm for Unsteady, Combined-Mode Heat Transfer Using the Discrete Ordinates Method

L.H. Howell
R.B. Pember
P. Colella
J.P. Jessee
W.A. Fiveland



UCRL-JC-132144
October 14, 1998

DISCLAIMER

This document was prepared as an account of work sponsored by an agency of the United States Government. Neither the United States Government nor the University of California nor any of their employees, makes any warranty, express or implied, or assumes any legal liability or responsibility for the accuracy, completeness, or usefulness of any information, apparatus, product, or process disclosed, or represents that its use would not infringe privately owned rights. Reference herein to any specific commercial product, process, or service by trade name, trademark, manufacturer, or otherwise, does not necessarily constitute or imply its endorsement, recommendation, or favoring by the United States Government or the University of California. The views and opinions of authors expressed herein do not necessarily state or reflect those of the United States Government or the University of California, and shall not be used for advertising or product endorsement purposes.

This work was performed under the auspices of the U.S. Dept. of Energy at LLNL under contract no. W-7405-Eng-48.

PREPRINT

This is a preprint of a paper that was submitted to *Numerical Heat Transfer, Part B: Fundamentals*. This preprint is made available with the understanding that it will not be cited or reproduced without the permission of the authors.

A Conservative Adaptive-Mesh Algorithm for Unsteady, Combined-Mode Heat Transfer Using the Discrete Ordinates Method

Louis H. Howell and Richard B. Pember

Center for Applied Scientific Computing, Lawrence Livermore National Laboratory
Livermore, CA 94550, USA

Phillip Colella

Applied Numerical Algorithms Group, Lawrence Berkeley National Laboratory
Berkeley, California 94720, USA

J. Patrick Jessee and Woodrow A. Fiveland

Research and Development Division, McDermott Technology, Inc.
Alliance, Ohio 44601, USA

Mailing address for proofs: Louis Howell, L-560

Lawrence Livermore National Laboratory
P.O. Box 808
Livermore, CA 94550

Abbreviated title: Adaptive Algorithm for Combined-Mode Heat Transfer

Abstract

Adaptive mesh refinement (AMR) permits a computational algorithm to allocate additional grid resolution when and where it is most needed. A block-structured AMR scheme provides this capability without sacrificing the numerical and computational efficiencies associated with regular meshes. In this paper we describe an AMR implementation of the discrete ordinates method for radiative transfer, coupled with an existing projection method for low-

Mach number flows. The complete algorithm constitutes a conservative scheme for unsteady combined-mode heat transfer. Results for two- and three-dimensional examples are shown.

Nomenclature

c_p	specific heat at constant pressure, kJ/kg·K
D_R	reflux divergence operator
e_{ij}	estimate of error in numerical solution in cell ij
\dot{E}^n	correction term in multilevel algorithm, J/(m ³ s)
h	enthalpy per unit mass, J/kg
I	instantaneous radiant intensity, W/(m ² · Sr)
\hat{I}_m^n	extension of I_m to coarse cells under fine grids
\tilde{I}_m^{n+1}	trial solution to I_m at new time level
$\bar{I}_m^{n+1/2}$	time-averaged intensity over a time step
\tilde{I}_m	nonphysical multilevel solution used to enforce energy conservation
I_b	blackbody intensity, $\sigma_b T^4/\pi$
L	length of pipe or duct in computational domain
$L_1^{\Delta x}$	estimate of error in numerical solution over entire domain
ℓ	level index
ℓ_{max}	level index of finest refinement level
m	ordinate index
N	conduction-radiation parameter, $\rho\kappa\lambda/4\sigma_b T_0^3$

n	time index
\hat{n}	outward unit normal at a boundary
Nu	Nusselt number, $2R\mathbf{q}_w/\lambda_0(T_b - T_w)$
\mathbf{P}	level projection operator
p	fluid pressure, kg/ms ²
Pr	Prandtl number, $\mu c_p/\lambda$
q	order of accuracy
r	refinement ratio between levels
r	radial (cylindrical) coordinate
\mathbf{q}_r	radiative heat flux, W/m ²
\mathbf{q}_w	total heat flux at wall, W/m ²
R	pipe radius or duct half-width, m
R_m	refluxing source at coarse-fine interfaces
Re	Reynolds number, $2R\rho u_0/\mu$
S	radiation source term, W/(m ³ · Sr)
T	temperature, K
T_b	bulk temperature, K
T_w	wall temperature, K
t	time, s
U	fluid velocity, m/s
u	x - component of velocity, m/s

u_0	mean inlet or initial axial velocity, m/s
v	y - (r -, if cylindrical) component of velocity, m/s
w	z - component of velocity, m/s
w_m	ordinate weight
x	axial coordinate
y, z	off-axis (Cartesian) coordinates

Greek symbols

$\delta I_m^{\ell+1}$	flux register for I_m at interface between levels ℓ and $\ell + 1$ (at level ℓ resolution)
Δt	size of a single time step, s
$\Delta x, \Delta y$	width, height of a computational cell
ϵ	wall emissivity
Θ	dimensionless time, $t\mu/R^2\rho\text{Pr}$
κ	absorption coefficient, m^{-1}
Λ_ℓ	collection of computation cells at refinement level ℓ
λ	thermal diffusivity, $\text{W}/\text{m}\cdot\text{K}$
$\partial\Lambda_\ell$	boundary between levels $\ell - 1$ and ℓ
μ	dynamic viscosity, $\text{kg}/\text{m}\cdot\text{s}$
μ, ξ, η	direction cosines
ρ	fluid density kg/m^3
ρ	wall reflectivity

σ	scattering coefficient, m^{-1}
σ_b	Stefan-Boltzmann constant, $5.669 \times 10^{-8} \text{W}/\text{m}^2 \text{ s}$
τ	optical thickness, κR
$\mathbf{\Omega}_m$	ordinate direction unit vector

Subscripts and superscripts

$(\cdot)_{ij}$	value at center of cell ij
$(\cdot)_{i,j+1/2}$	value at upper y -edge of cell ij
$(\cdot)^n$	value at time t^n
$(\cdot)^{n+1}$	value at time $t^n + \Delta t = t^{n+1}$
$(\cdot)^{n+1,p}$	predicted value at center of time t^n
$(\cdot)^{n+1/2}$	value at time $t^n + \Delta t/2$
$(\cdot)_{i+1/2,j}$	value at upper x -edge of cell ij
0	initial or inlet values
w	wall values

Other

$\langle \cdot \rangle$	average from fine to coarse level, space only
$\langle \langle \cdot \rangle \rangle$	average from fine to coarse level, space and time

Introduction

The computational modeling of practical combustion applications with limited computer resources can be made difficult by the presence of multiple length scales and high gradients and by the large number of species in a sufficiently detailed reaction mechanism. In addition,

the locations of regions with high gradients or small length scales may change over time. An accurate prediction of a reacting flow may therefore require that the computational grid be dynamically adapted both in time and space.

Radiative heat transfer is the dominant mode of heat transfer in many combustion applications. Because it can significantly affect temperatures, and, hence, density distributions and reaction rates, radiative heat transfer may be very influential in combustion dynamics. Deterministic methods for radiative heat transfer have been formulated for globally refined, nonuniform grids (see, for example, [1]). However, most of these methods use fixed computational grids and are appropriate only for steady flows.

In this paper we present a method based on a different approach, local adaptive mesh refinement (AMR). We develop an AMR algorithm to solve a system of equations for unsteady combined-mode heat transfer, using a hierarchical grid structure approach first developed by Berger and Oliger [2] and Berger and Colella [3] for hyperbolic conservation laws in two dimensions, and extended to three dimensions by Bell *et al.* [4]. The grid structure is dynamic in time and is composed of nested uniform rectangular grids of varying resolution. By using grids of finer resolution in both space and time in the regions of most interest, AMR allows one to model large problems more efficiently. The integration algorithm on the grid hierarchy is a recursive procedure in which a coarse grid is advanced, fine grids are advanced multiple steps to reach the same time as the coarse grid, and the coarse and the fine grids are synchronized. The method is valid for multiple grids on each level and for multiple levels of refinement.

The central feature of the algorithm presented here is a new scheme for modeling unsteady radiative transport with a discrete ordinates method [5, 6, 7] on locally refined meshes. This

scheme incorporates portions of the adaptive mesh refinement discrete ordinates algorithm for solving instantaneous or steady-state radiative heat transfer problems described in [8]. The method is also based on two other earlier works, an incompressible adaptive mesh refinement algorithm (IAMR) [9] and a single grid projection method for unsteady low-Mach number combustion [10].

The remainder of this paper is broken into four sections. The first section presents the governing equations. The second section discusses the numerical method, including a review of the three works on which it is based. The third section presents and discusses numerical results computed with the algorithm. The last section summarizes the work and discusses future directions.

Governing Equations

We make the following simplifications for the sake of exposition. The fluid is an incompressible single component gas with constant and uniform density, viscosity, thermal diffusivity, and specific heat. Body forces and the heat production due to viscous stress are negligible. The governing equations for unsteady combined mode heat transfer are then the following:

$$\frac{\partial U}{\partial t} + (U \cdot \nabla)U = \frac{1}{\rho}(-\nabla p + \mu \nabla^2 U) \quad (1)$$

$$\frac{\partial \rho c_p T}{\partial t} + \nabla \cdot \rho U c_p T = \lambda \nabla^2 T - \nabla \cdot \mathbf{q}_r \quad (2)$$

$$\nabla \cdot U = 0. \quad (3)$$

Eq. (2) is written in conservative form to underscore the fact that the algorithm described below conserves enthalpy.

This paper considers an emitting-absorbing and isotropically scattering gray medium, although the discrete ordinates method is not restricted to these conditions. For this medium, the radiative transfer equation (RTE) is

$$(\boldsymbol{\Omega} \cdot \nabla) I(\boldsymbol{\Omega}) + (\kappa + \sigma)I(\boldsymbol{\Omega}) = \kappa I_b + \frac{\sigma}{4\pi} \int_{4\pi} I(\boldsymbol{\Omega}') d\boldsymbol{\Omega}'. \quad (4)$$

The divergence of the radiative heat flux is given by

$$\nabla \cdot \mathbf{q}_r = 4\pi\kappa I_b - \kappa \int_{4\pi} I(\boldsymbol{\Omega}') d\boldsymbol{\Omega}'. \quad (5)$$

For gray surfaces which reflect diffusely, the radiative boundary condition for (4) is given by

$$I(\boldsymbol{\Omega}) = \epsilon I_b + \frac{\rho}{\pi} \int_{\hat{n} \cdot \boldsymbol{\Omega}' > 0} (\hat{n} \cdot \boldsymbol{\Omega}') I(\boldsymbol{\Omega}') d\boldsymbol{\Omega}' \quad (6)$$

for $\hat{n} \cdot \boldsymbol{\Omega} < 0$ where $I(\boldsymbol{\Omega})$ is the intensity leaving the surface and ρ is the surface reflectivity.

Numerical Algorithm

The algorithm is derived from three previous works: an incompressible adaptive mesh refinement (IAMR) algorithm [9], a single grid projection method for low-Mach number combustion [10], and an adaptive mesh refinement discrete ordinates algorithm for solving instantaneous or steady-state radiative heat transfer problems [8]. In the next three subsections, we briefly review these in the context of this paper in order to lay the groundwork for the discussion of the AMR scheme for unsteady radiative heat transfer in the fourth subsection. In the fifth subsection, we briefly discuss extensions to flows with variable properties.

AMR for Unsteady Convective Heat Transfer

IAMR [9] solves the unsteady Navier-Stokes equations for incompressible flow (Eqs. (1) and (3)) along with additional equations for convected and diffused scalars on a block-structured adaptive mesh. For the discussion here, we consider one such additional equation, the energy equation for unsteady convective heat transfer:

$$\frac{\partial \rho c_p T}{\partial t} + \nabla \cdot \rho U c_p T = \lambda \nabla^2 T. \quad (7)$$

The IAMR algorithm uses a hierarchical grid structure, which changes dynamically in time, composed of rectangular, uniform grids of varying resolution. The collection of grids at a given resolution is referred to as a level, and is denoted by Λ^ℓ for $\ell \in \{0, 1, 2, \dots\}$. Level 0 is the coarsest level and covers the entire problem domain. The widths of the cells in the level ℓ grids differ from those at $\ell + 1$ by a even integer factor r_ℓ called the refinement ratio; r_ℓ is typically 2 or 4. In space, the levels are properly-nested, i.e., there must always be a region at least one cell wide at level $\ell + 1$ separating two levels ℓ and $\ell + 2$. The algorithm is implemented for Cartesian (two- and three-dimensional) and axisymmetric coordinates. For simplicity we restrict most of the discussion in this paper to two-dimensional Cartesian coordinates.

(It is useful at this point to define a level projection operator \mathbf{P} for later use in the paper. $\mathbf{P}(\Lambda^{\ell+1})$ is the collection of cells at level ℓ covered by cells at level $\ell + 1$; $\Lambda^\ell - \mathbf{P}(\Lambda^{\ell+1})$ is the portion of level ℓ that is not covered. Similarly, $\mathbf{P}(\partial\Lambda^{\ell+1})$ is the collection of level ℓ cell edges covered by $\partial\Lambda^{\ell+1}$, the border of level $\ell + 1$.)

Two features of the IAMR algorithm must be outlined here in order to show how the radiative transfer scheme fits into it. These are the single-level timestep and the adaptive-

mesh timestep. At a single level ℓ , the basic IAMR timestep to advance the solution from time t^n to time $t^n + \Delta t = t^{n+1}$ proceeds as follows. Convective derivatives $(U \cdot \nabla U)_{ij}^{n+1/2}$ and $(\nabla \cdot UT)_{ij}^{n+1/2}$ are computed at cell centers at time $n + 1/2$ using a second-order Godunov method [11] and MAC-projected edge velocities. The solution of Crank-Nicholson difference equations for (7) and (1) then computes T and U at time $n + 1$. We solve

$$\rho c_p \left(\frac{T_{ij}^{n+1} - T_{ij}^n}{\Delta t} + (\nabla \cdot UT)_{ij}^{n+1/2} \right) = \frac{\lambda}{2} \left((\nabla^2 T)_{ij}^n + (\nabla^2 T)_{ij}^{n+1} \right) \quad (8)$$

and a similar equation for velocity. Because the computed velocity does not necessarily satisfy (3), a projection [12] is applied to correct the velocity and update the pressure.

On the full adaptive mesh, an IAMR timestep consists of separate timesteps on each of the levels, plus synchronization operations to insure correct behavior at the coarse-fine interfaces, plus regridding operations which permit the refined grids to track complex and/or interesting regions of the flow. The ratio of the level ℓ and the level $\ell + 1$ time steps is r_ℓ , so that the Courant number is roughly the same on all levels. The timestep is a recursive procedure which proceeds as follows on level ℓ :

1. Advance level ℓ , using boundary information from level $\ell - 1$ as needed but ignoring levels $\ell + 1$ and higher.
2. Advance level $\ell + 1$ r_ℓ times. (This involves advancing levels $\ell + 2$ and higher, recursively.)
3. Synchronize levels ℓ and $\ell + 1$.
4. At appropriate intervals, generate new level $\ell + 1$ grids.

The synchronization operations serve in part to ensure that the overall timestepping scheme conserves enthalpy. The operations are otherwise complex and mostly irrelevant to

the unsteady radiative transfer algorithm. The only part we describe here is the *refluxing* operation for the convective terms: During a coarse timestep, both coarse and fine grids compute convective fluxes on the faces that make up the coarse-fine interface. Since these fluxes do not match exactly, it is necessary to adjust the flux computed on the coarse grid to bring it into agreement with the integrated fluxes from the fine grid in order to insure conservation. For convection, it is then sufficient to adjust the state in coarse cells bordering a fine grid to account for the new flux information. The key data structure for refluxing is an object called the *flux register*, that exists at coarse-fine interfaces at the same resolution as the coarse grid.

Though the synchronization operations for the elliptic and parabolic portions of the algorithm are more complicated, they also depend on flux registers for storing information about various imbalances between coarse and fine grids. We likewise use these data structures for storing information relevant to energy conservation in the radiative transfer algorithm.

Single Grid Algorithm for Unsteady Combined Mode Heat Transfer

A single grid projection method for low-Mach number combustion is described in [10]. The application of this algorithm to Eqs. (1)–(5) essentially follows the same steps as the single level algorithm described above with the following changes. A term approximating $\nabla \cdot \mathbf{q}_r$ at time $n + 1/2$ is subtracted from the right hand side of (8). The resulting temperature equation is solved in a predictor-corrector fashion in order to time-center the radiative term. We first solve the equation using $(\nabla \cdot \mathbf{q}_r)_{ij}^n$ for the half-time divergence. We then compute $(\nabla \cdot \mathbf{q}_r)_{ij}^{n+1}$ using the temperature just found. We then solve the temperature equation again using $1/2 \left((\nabla \cdot \mathbf{q}_r)_{ij}^n + (\nabla \cdot \mathbf{q}_r)_{ij}^{n+1} \right)$.

AMR Discrete Ordinates for Steady Radiative Transport

We now summarize the AMR discrete ordinates algorithm for solving instantaneous or steady-state radiative transfer problems presented in [8].

The instantaneous radiation field satisfies the radiative transfer equation (4). The discrete ordinate method is based on a semi-discrete form of this equation,

$$(\mathbf{\Omega}_m \cdot \nabla) I_m + (\kappa + \sigma) I_m = \kappa I_b + \frac{\sigma}{4\pi} \sum_{m'} w_{m'} I_{m'}, \quad (9)$$

where the continuous dependence of the radiative intensity I on angle is reduced to consideration only of the intensity in the discrete directions $\mathbf{\Omega}_m$. The ordinate weights w_m satisfy $\sum w_m = 4\pi$. The corresponding discretization of (5) is

$$\nabla \cdot \mathbf{q}_r = \sum_m w_m \kappa (I_b - I_m) = 4\pi \kappa I_b - \sum w_m \kappa I_m. \quad (10)$$

Discretizing (9) conservatively over cells gives, in Cartesian coordinates,

$$\begin{aligned} \frac{\mu_m}{\Delta x} (I_{m,i+\frac{1}{2},j} - I_{m,i-\frac{1}{2},j}) + \frac{\xi_m}{\Delta y} (I_{m,i,j+\frac{1}{2}} - I_{m,i,j-\frac{1}{2}}) \\ + (\kappa + \sigma) I_{m,ij} = S_m(I), \end{aligned} \quad (11)$$

where the emission and scattering sources have been combined into a single source term $S_m(I)$. The system can be closed by specifying a relationship between the cell and the edge values, such as the diamond-difference or step approximation, but the multilevel algorithm does not depend on the details of this relationship. Finally, Eq. (6) is discretized to provide a physical boundary condition at exterior faces, combining the effects of emission and diffuse reflection at the walls:

$$I_m = \epsilon I_b^{\text{wall}} + \frac{\rho}{\pi} \sum_{\hat{n} \cdot \mathbf{\Omega}_{m'} > 0} w_{m'} (\hat{n} \cdot \mathbf{\Omega}_{m'}) I_{m'}, \quad \hat{n} \cdot \mathbf{\Omega}_m < 0. \quad (12)$$

Note that the intensities I_m in different ordinate directions are coupled only through the scattering term and through reflection at the boundary. Eqs. (9) and (12) are solved by repeatedly sweeping through the grid for all ordinate directions. For each ordinate the sweep proceeds in the direction the radiation is moving. After each sweep the reflection and scattering sources are updated, and the iteration is continued until the system converges. If scattering is isotropic the source $S_m(I)$ is independent of direction and it is not necessary to maintain storage for all ordinate directions at once. (It is convenient, though, to allocate storage for edge fluxes at the boundary for all ordinate directions.)

So far we have described the discrete ordinates method as it has been presented in many earlier sources [5, 6, 7]. The contribution of [8] was to extend this method to the adaptive grid structure described above. In each uniform region Λ_ℓ of the adaptive mesh, the solution satisfies equation (11) in the interior and the boundary condition (12) at the walls. At a coarse-fine interface $\partial\Lambda^{\ell+1}$ we require the coarse flux to be the average of the fine fluxes across each face:

$$I_m^\ell = \langle I_m^{\ell+1} \rangle \quad \text{on } \mathbf{P}(\partial\Lambda^{\ell+1}). \quad (13)$$

There are two new features added to the computation in order to deal with the adaptive mesh. One is the sequencing of grids on each individual level, the other is the method of cycling between levels to obtain a converged solution. The single-level algorithm is just an elaboration of that for a single grid: transport sweeps are performed for each ordinate in the direction of propagation. This imposes an ordering on the grids, since some grids must be solved before others. In two dimensions, the necessary orderings always exist, and to handle all ordinate directions a total of four orderings are required (one for transport towards the

upper right, one towards the lower right, and the reversals of these for transport to the left).

In three dimensions, however, there are cases where an ordering is not possible (this complication was not mentioned in [8]). We resolve the difficulty by dividing grids into pieces. A situation in which the ordering of three adjacent grids is ill-defined can be resolved by dividing any of the three grids into two parts; the resulting four grids can then be ordered appropriately. A total of eight orderings are required in three dimensions, of which four are reversals of the other four.

The situation becomes more complicated when multiple levels are involved. Radiation passes from coarse to fine grids on the upstream edges of the fine grids, and from fine to coarse grids on the downstream edges. We compute the composite solution across all levels by again iterating a transport process until the system converges. The process now covers all active levels, however, in sequence from coarse to fine and back again.

The details of the multilevel iteration are not as important as the form of the resulting solution. We obtain at each level ℓ a solution I_m^ℓ satisfying (9) on the exposed portion of the level $\Lambda^\ell - \mathbf{P}(\Lambda^{\ell+1})$, satisfying (12) on physical boundaries, and satisfying (13) on $\mathbf{P}(\partial\Lambda^\ell)$ and $\mathbf{P}(\partial\Lambda^{\ell+1})$. On interfaces where radiation passes from a coarse grid to a fine grid we enforce (13) trivially by setting $I_m^{\ell+1} := I_m^\ell$. Transport sweeps across a level do not stop when a finer level is encountered, however. There is therefore an extended solution \hat{I}_m^ℓ , which agrees with I_m^ℓ in the exposed region where that exists, but is also defined in the region $\mathbf{P}(\Lambda^{\ell+1})$ under the finer level.

This extended solution obeys an equation

$$(\mathbf{\Omega}_m \cdot \nabla) \hat{I}_m + (\kappa + \sigma) \hat{I}_m = S_m(\hat{I}) - D_R(\mathbf{\Omega}_m \delta I_m^{\ell+1}) \quad (14)$$

over all of Λ^ℓ . The final term in this equation can be thought of as feeding fine grid information back into the coarse grid. $\delta I_m^{\ell+1}$ is accumulated in flux registers and is defined as

$$\delta I_m^{\ell+1} = \langle I_m^{\ell+1} \rangle - \hat{I}_m^\ell \quad \text{on } \mathbf{P}(\partial\Lambda^{\ell+1}). \quad (15)$$

(Note that $\delta I_m^{\ell+1} = 0$ along the upstream faces where radiation enters the fine grid.) D_R is the “reflux divergence” operator, which returns the divergence of its argument on the coarse cells bordering $\partial\Lambda^{\ell+1}$. The effect of this term is to enforce equation (13) along the downstream faces where radiation passes from the fine to the coarse grid.

AMR for Time-dependent Radiative Transfer

The AMR algorithm for unsteady combined-mode heat transfer differs from the convective transport algorithm in two significant ways. The first is simply that it incorporates the predictor-corrector treatment of the temperature equation described above for the single grid algorithm for combined mode heat transfer. The second difference entails the incorporation of the discrete ordinates algorithm. The remainder of this subsection focuses on this topic.

For a time step in a single level calculation, i.e., one in which $\ell_{max} = 0$, we solve for I_m at times n and $n + 1$, compute $(\nabla \cdot \mathbf{q}_r)^n$ and $(\nabla \cdot \mathbf{q}_r)^{n+1}$, and then update T in a time-centered fashion so that the scheme is second-order in time. Note that this update is automatically conservative, since it involves a simple integration in time of a conservative radiative transport solution for the entire domain. In the multilevel adaptive algorithm, however, the domain is not all advanced at a single time step, and imbalances in the radiative energy field develop along level interfaces which must be stored and redistributed properly in order for the scheme to be conservative.

The multilevel algorithm is specified recursively by detailing the interactions of a single level ℓ with the levels both above and below in the hierarchy, as it advances from time index n to $n + 1$. (In our description, we do not distinguish time indices on other levels, though we point out that many finer-level time steps are involved.) Before we provide the equations, though, it may be helpful to describe the basic form of the algorithm and the roles played by the important variables.

We begin a coarse time step by computing a multilevel solution I_m^n across all the active levels. Note that this defines $(\nabla \cdot \mathbf{q}_r)^n$ at level ℓ and all finer levels. We then advance the coarse level. We first compute a predicted temperature $T^{n+1,p}$ on level ℓ . We next compute a trial solution \tilde{I}_m^{n+1} at the new time, approximating the effect of the missing finer levels on the coarse region $\Lambda^\ell - \mathbf{P}(\Lambda^{\ell+1})$ by reusing the reflux contribution from time n . We find $(\nabla \cdot \mathbf{q}_r)^{n+1}$ using the values of \tilde{I}_m^n and compute T^{n+1} .

The coarse cells in the fine region $\mathbf{P}(\Lambda^{\ell+1})$ are eventually overwritten by finer level data. Changes to the fluid state in this region affects cells outside the coarse-fine interface, however, so we also modify the enthalpy update in $\mathbf{P}(\Lambda^{\ell+1})$ with an estimate of the effects of levels $\ell + 1$ and above. A quantity $\dot{E}^{\ell+1}$ is computed for this purpose from the time n multilevel solution, and is used in the coarse enthalpy update. These attempts to anticipate the effects of the finer levels are used only to improve accuracy—none are needed for conservation, as that is provided by the synchronization procedure at the end of the coarse time step. Note that by definition, $\dot{E}^{\ell+1} = 0$ on $\Lambda^\ell - \mathbf{P}(\Lambda^{\ell+1})$ and on $\Lambda^{l_{max}}$.

Once the trial solution to level ℓ is in place at time $n + 1$, level $\ell + 1$ is advanced through r cycles to bring it up to the same time. (Recall that this procedure in turn involves advancing and regridding still finer levels, if any.) Boundary conditions for level $\ell + 1$ are obtained by

interpolating the level ℓ solution in both space and time. For the radiative intensity I_m we use piecewise linear interpolation in time and piecewise constant interpolation in space, so the fine flux at each incoming face is set to the time-weighted average of the fluxes at the corresponding coarse faces. Outgoing fluxes at the coarse-fine interface are accumulated in flux registers for use in the synchronization step.

At the end of a coarse time step we perform the radiation synchronization step. (This step follows all the other AMR synchronizations.) We compute two multilevel solutions. One is simply the new-time radiative transfer solution I_m^{n+1} , which is also used as the baseline solution for the next time step. The other is computed with the accumulated coarse-fine flux mismatch used as an additional source term. The difference between these solutions is applied to all active levels to insure conservation of energy. (The correction is computed in this manner because it can be negative as well as positive, but the method we use to solve the discrete ordinates equations on each grid has a limiter that disallows negative fluxes.)

When more than two levels begin or end together, the multilevel computations are combined. Consider, for example, a calculation with two levels of refinement. The end of a level 1 timestep requires synchronization of levels 1 and 2. If the level 0 step is also completed, however, we perform a single synchronization operation for levels 0, 1 and 2 together. Note that a synchronization of levels 1 and 2 also contributes an increment to the flux registers at the 0-1 interface, which will be part of the source at the next 0-1-2 synchronization.

We are now ready to formally specify the details of the radiative transfer algorithm for advancing a level ℓ . Note that the multilevel solve at the initialization step has to be performed only if level ℓ was regridded just prior to the beginning of the time step, and then only if it has not already been done for this time by a still coarser level than the current

one. This is checked by comparing the time stamps for the current level to that of the next coarser one. Also note that the synchronization step does not have to be done if it is going to be done by a still coarser level that has been updated to the same time. Again, this is checked by comparing time stamps.

If $(\ell = 0 \text{ or } t^{\text{old},\ell} > t^{\text{old},\ell-1})$ **then**

Initialization from coarsest to finest level at current time, levels $\ell' \in \{\ell, \dots, \ell_{\max}\}$:

For $\ell' \in \{\ell_{\max} - 1, \dots, \ell\}$ **do**

- $I_b^{\ell',n} := \langle I_b^{\ell'+1,n} \rangle$ on $\mathbf{P}(\Lambda^{\ell'+1})$

Enddo

Multilevel Solve: $\ell' \in \{\ell, \dots, \ell_{\max}\}$

(Omit this computation if a valid solution is already available from the end of the previous time step.)

- $(\boldsymbol{\Omega}_m \cdot \nabla) I_m^{\ell',n} = \kappa I_b^{\ell',n} - (\kappa + \sigma) I_m^{\ell',n} + S_m(I^{\ell',n})$ on $\Lambda^{\ell'} - \mathbf{P}(\Lambda^{\ell'+1})$
- $I_m^{\ell',n} = \langle I_m^{\ell'+1,n} \rangle$ on $\mathbf{P}(\partial\Lambda^{\ell'+1})$, $\ell' < \ell_{\max}$

End

For $\ell' \in \{\ell, \dots, \ell_{\max} - 1\}$ **do**

- Derive $(\boldsymbol{\Omega}_m \cdot \nabla) \hat{I}_m^{\ell',n} = \kappa I_b^{\ell',n} - (\kappa + \sigma) \hat{I}_m^{\ell',n} + S_m(\hat{I}^{\ell',n}) - D_R(\boldsymbol{\Omega}_m \delta I_m^{\ell'+1,n})$ on $\Lambda^{\ell'}$
- $\delta I_m^{\ell'+1,n} := \langle I_m^{\ell'+1,n} \rangle - \hat{I}_m^{\ell',n}$ on $\mathbf{P}(\partial\Lambda^{\ell'+1})$
- $\dot{E}^{\ell'+1,n} := \sum_m w_m \kappa (\langle I_m^{\ell'+1,n} \rangle - \hat{I}_m^{\ell',n})$ on $\mathbf{P}(\Lambda^{\ell'+1})$
- Compute $(\nabla \cdot \mathbf{q}_r)^n$ using $\hat{I}_m^{\ell',n}$

Enddo

Endif

Time step, level ℓ :

- Compute the predicted temperature $T^{n+1,p}$ by solving

$$\rho c_p \left(\frac{T_{ij}^{n+1,p} - T_{ij}^n}{\Delta t} + (\nabla \cdot UT)_{ij}^{n+1/2} \right) = \frac{\lambda}{2} \left((\nabla^2 T)_{ij}^n + (\nabla^2 T)_{ij}^{n+1,p} \right) - (\nabla \cdot \mathbf{q}_r)^n + \dot{E}^{\ell'+1,n}$$

- Using $T^{n+1,p}$, solve

$$(\mathbf{\Omega}_m \cdot \nabla) \check{I}_m^{\ell,n+1} = \kappa I_b^{\ell,n+1} - (\kappa + \sigma) \check{I}_m^{\ell,n+1} + S_m(\check{I}^{\ell,n+1}) - D_R(\mathbf{\Omega}_m \delta I_m^{\ell+1,n}) \text{ on } \Lambda^\ell$$

- $\bar{I}_m^{\ell,n+1/2} := 1/2(\hat{I}_m^{\ell,n} + \check{I}_m^{\ell,n+1})$
- Compute $(\nabla \cdot \mathbf{q}_r)^{n+1}$ using $\check{I}_m^{\ell,n+1}$
- Compute the corrected temperature T^{n+1} by solving

$$\rho c_p \left(\frac{T_{ij}^{n+1,p} - T_{ij}^n}{\Delta t} + (\nabla \cdot UT)_{ij}^{n+1/2} \right) = \frac{\lambda}{2} \left((\nabla^2 T)_{ij}^n + (\nabla^2 T)_{ij}^{n+1,p} \right) - \frac{1}{2} \left((\nabla \cdot \mathbf{q}_r)^n + (\nabla \cdot \mathbf{q}_r)^{n+1} \right) + \dot{E}^{\ell'+1,n}$$

- Advance levels $\ell + 1, \dots, \ell_{\max}$.
- $\delta \bar{I}_m^{\ell+1,n+1/2} := \langle \langle \bar{I}_m^{\ell+1} \rangle \rangle - \bar{I}_m^{\ell,n+1/2}$ on $\mathbf{P}(\partial \Lambda^{\ell+1})$

If ($\ell = 0$ or $t^{\text{new},\ell} < t^{\text{new},\ell-1}$) **then**

Synchronization/refluxing, levels $\ell' \in \{\ell, \dots, \ell_{\max}\}$:

For $\ell' \in \{\ell_{\max} - 1, \dots, \ell\}$ **do**

- $I_b^{\ell', n+1} := \langle I_b^{\ell'+1, n+1} \rangle$ on $\mathbf{P}(\Lambda^{\ell'+1})$
- $R_m^{n+1} := -D_R(\mathbf{\Omega}_m(\delta \bar{I}_m^{\ell'+1, n+1/2} - \delta I_m^{\ell'+1, n})) \cdot (\Delta t^{\ell'} / \Delta t^{\ell})$ on $\mathbf{P}(\partial \Lambda^{\ell'+1})$

Enddo

Multilevel Solve: $\ell' \in \{\ell, \dots, \ell_{\max}\}$

- $(\mathbf{\Omega}_m \cdot \nabla) \tilde{I}_m^{\ell', n+1} = \kappa I_b^{\ell', n+1} - (\kappa + \sigma) \tilde{I}_m^{\ell', n+1} + S_m(\tilde{I}_m^{\ell', n+1}) + R_m^{n+1}$ on $\Lambda^{\ell'} - \mathbf{P}(\Lambda^{\ell'+1})$
- $\tilde{I}_m^{\ell', n+1} = \langle \tilde{I}_m^{\ell'+1, n+1} \rangle$ on $\mathbf{P}(\partial \Lambda^{\ell'+1})$, $\ell' < \ell_{\max}$

End

Multilevel Solve: $\ell' \in \{\ell, \dots, \ell_{\max}\}$

- $(\mathbf{\Omega}_m \cdot \nabla) I_m^{\ell', n+1} = \kappa I_b^{\ell', n+1} - (\kappa + \sigma) I_m^{\ell', n+1} + S_m(I_m^{\ell', n+1})$ on $\Lambda^{\ell'} - \mathbf{P}(\Lambda^{\ell'+1})$
- $I_m^{\ell', n+1} = \langle I_m^{\ell'+1, n+1} \rangle$ on $\mathbf{P}(\partial \Lambda^{\ell'+1})$, $\ell' < \ell_{\max}$

End

For $\ell' \in \{\ell_{\max} - 1, \dots, \ell\}$ **do**

- $(\rho c_p T)^{\ell', n+1} := (\rho c_p T)^{\ell', n+1} + \Delta t^{\ell'} \sum_m w_m \kappa (\tilde{I}_m^{\ell', n+1} - I_m^{\ell', n+1})$ on $\Lambda^{\ell'} - \mathbf{P}(\Lambda^{\ell'+1})$
- $(\rho c_p T)^{\ell', n+1} := \langle (\rho c_p T)^{\ell'+1, n+1} \rangle$ on $\mathbf{P}(\Lambda^{\ell'+1})$

Enddo

- $\bar{I}_m^{\ell, n+1/2} := \bar{I}_m^{\ell, n+1/2} + (\tilde{I}_m^{\ell, n+1} - I_m^{\ell, n+1})$ on $\mathbf{P}(\partial \Lambda^{\ell})$, $\ell > 0$

Endif

Note that the final enthalpy update can be written in the form

$$\rho c_p T := \rho c_p T + \Delta t \sum_m w_m ((\mathbf{\Omega}_m \cdot \nabla) \tilde{I}_m - (\mathbf{\Omega}_m \cdot \nabla) I_m - R_m). \quad (16)$$

The first two terms in the sum are fluxes, and thus have no effect on global energy conservation. The final term (R_m) undoes the failure to conserve energy due to the mismatch of fluxes at the coarse-fine grid interfaces and the inclusion of the D_R term in the level solve.

The composite solution \tilde{I}_m^{n+1} does not have a clear physical interpretation. We are only interested in its difference with I_m^{n+1} , which we compute in this way to avoid problems with the limiter. In the description above, there are three calls to the multilevel solver. As noted, however, the first call is necessary only if the grid structure has been changed, rendering the previous solution to I_m^n invalid.

Extensions to Variable Properties

The extension of the algorithm described above to allow for gravity, multiple species, kinetics, compressibility, and variable density, thermal diffusivity, specific heat, and viscosity follows the approach described in [10, 13]. Spatial and temporal variation of the absorption and scattering coefficients are already accounted for in the description above. For multi-group radiation, we consider only absorbing-emitting media. We follow the approach in [14]: each band is solved separately and the contributions of the individual bands are summed. Each band requires its own set of flux registers. This represents the only increase in memory requirements over a gray gas approach.

Numerical Examples

In this section we present four numerical examples computed using the adaptive mesh algorithm for unsteady, combined-mode heat transfer described above. We first show three sets

of results to validate the algorithm: simultaneously developing axisymmetric pipe flow, simultaneously developing three-dimensional flow in a square duct, and, finally, a shearing flow in a closed box to demonstrate that the algorithm is conservative with a complex adaptive grid structure. In the fourth example, we combine our algorithm with an adaptive algorithm for unsteady low-Mach combustion [13] to compute a flickering laminar flame.

Except as noted, we make the following assumptions and strategies. The computational cells are square and a Courant number of 0.5 is used. Physical properties are uniform and constant in time within each example, and the flow is incompressible. The results with radiation are obtained using the step approximation. We use an S_6 ordinate set in a convergence study and otherwise use S_4 . Both sets are tabulated in [15], and are chosen because they have correct half-range first moments and therefore conserve energy at the boundaries.

With respect to radiation, symmetry boundary conditions are used at flow exits, while inlets are treated as nonreflecting walls at the inflow temperature. In all but the third example, we assume black walls, i.e., $\epsilon = 1$. In the third example the walls are all perfect diffuse reflectors ($\epsilon = 0$, $\rho = 1$), so the heat content of the box is constant in time.

Simultaneously Developing Laminar Pipe Flow

The first example is an axisymmetric computation of simultaneously developing laminar flow in the entry region of a pipe. The initial and inlet axial velocities and temperature are both uniform, $u = u_0$ and $T = T_0$, respectively. The temperature at the wall of the pipe is $T = T_w$. We compute the flow on the domain $0 \leq r \leq R$, $0 \leq x \leq L = .3R\text{RePr} = 8R$. For the results shown here, $\text{Re} = 35.086$, $\text{Pr} = .76$, $N = 1$, $\tau = 1$ and $T_w/T_0 = 1.5$. The

steady-state solution is found by timestepping until a time independent solution is achieved ($\Theta \approx .55$). We then compare this numerical solution with the steady-state boundary layer solution obtained by Pearce and Emery [16].

We compute results for a uniform grid and five different adaptive grid hierarchies. The six cases, including the uniform grid case, are:

- 1) 64×512 level 0 grid, $\ell_{max} = 0$
- 2) 32×256 level 0 grid, $\ell_{max} = 1, r_0 = 2$
- 3) 16×128 level 0 grid, $\ell_{max} = 1, r_0 = 4$
- 4) 16×128 level 0 grid, $\ell_{max} = 2, r_0 = 2, r_1 = 2$
- 5) 8×64 level 0 grid, $\ell_{max} = 2, r_0 = 2, r_1 = 4$
- 6) 4×32 level 0 grid, $\ell_{max} = 2, r_0 = 4, r_1 = 4$.

The refinement strategy in cases 2–6 is to tag all cells for which $x/L < .0625$ and those cells for which $x/L < .375$ and $.3 \leq (T - T_0)/(T_w - T_0) \leq .7$. Note that with this strategy, the grids change in time as the temperature solution evolves. Note also that if the refinement strategy were instead to refine everywhere, the finest level would consist of a 64×512 grid covering the entire domain in all five adaptive cases. Fig. 1 compares the computed bulk temperature at steady-state ($\Theta = .55$) for case 6 with the Pearce-Emery results; the bulk temperature curves for the other five cases are indistinguishable from the case 6 profile. Fig. 2 compares the computed Nusselt numbers (based on total heat flux at the pipe wall) for cases 1, 4, 5, and 6 with the Pearce-Emery results; cases 2 and 3 are indistinguishable from case 1. Fig. 3 shows a time history of the normalized temperature field for case 6. The temperature and grid boundaries are displayed at $\Theta = .06875, .1375, .275$ and $.55$.

The computed results and the Pearce-Emery predictions are in fairly good agreement.

The computed Nusselt numbers show greater disagreement with the Pearce-Emery results than the bulk temperatures. The differences may be due to the fact that Pearce and Emery make two approximations which we do not. Specifically, in [16] the wall is considered to be an infinite tube at $T = T_w$, and axial temperature variations are neglected in the computation of $\nabla \cdot q_{rad}$. The Nusselt number profiles for all six strategies are in close agreement with one another except in the region where no refinement occurs, i.e., $(x/R)/RePr > .1125$. In other words, the discrepancies in the curves are due simply to differences in resolution in the unrefined region.

We now present timings of the code for the six gridding strategies. The calculations were all run on a single 533 Mhz processor of a DEC Alpha workstation to a final time of $\Theta = .55$. Table 1 shows the CPU time used to complete the calculation, the CPU time per cell per level timestep advance, the percentage CPU time for radiation, and the approximate peak memory usage. We note that the average percentage of the domain refined to the finest level is roughly the same in each case — 22% for cases 2, 5, and 6, 25% for case 4, and 27% for case 3.

The numbers in table 1 show that the adaptive mesh refinement scheme can reduce the computational cost in terms of both CPU time and memory usage. For this particular problem and refinement strategy, cases 4, 5, and 6 show the best reduction in computational cost over the uniform grid calculation. In these cases, a substantially smaller proportion of time ($\sim 10\%$) was spent on multilevel solves than in cases 2 and 3 ($\sim 20\%$). The comparative advantage of the latter three cases is most likely due, then, to the fact that each uses relatively less CPU time on multilevel solves, which is in turn due to the use of one or more refinement ratios of 4. The AMR timestepping scheme requires two multilevel solves for every r fine

time steps, so the overhead due to multilevel solves is smaller for cases 4, 5 and 6 than for cases 2 and 3.

We finally show results to confirm that the algorithm is spatially and temporally second order accurate. The MINMOD scheme is used here [17, 18] instead of the step scheme because the latter is only first order accurate. We compute solutions on 4×32 , 8×64 , 16×128 , and 32×256 uniform grids. The errors in the solution on the three coarser grids are computed at $\Theta = .06875$, $.1375$, $.275$, and $.55$. Because there is no exact solution, we estimate the error in the numerical solution by comparing solutions at successive resolutions. We first compute the error e_{ij} in a single coarse grid computational cell as the difference of the coarse grid result and the average of the solution in the overlying fine grid cells. The L_1 error on the entire coarse domain (assuming $\Delta x = \Delta y$) is then defined by

$$L_1^{\Delta x} = \sum_{ij} (\Delta x)^2 e_{ij}.$$

The convergence rate q can then be computed by comparing errors at successive resolutions:

$$q = \log_2 \left(L_1^{2\Delta x} / L_1^{\Delta x} \right).$$

The errors and convergence rates are shown in table 2. The results show that the numerical algorithm is second-order accurate for this problem.

Simultaneously Developing Three-Dimensional Duct Flow

The second example is a three-dimensional calculation of simultaneously developing laminar flow in the entry region of a square duct. The initial and inlet axial velocities and temperature are both uniform, $u = u_0$ and $T = T_0$, respectively. The temperature at the wall of the pipe is $T = T_w$. We compute the flow on the domain $0 \leq y, z \leq R$, $0 \leq x \leq L = .6R\text{RePr} = 42R$.

Symmetry boundary conditions are used at $y = 0$ and $z = 0$. For the results shown here, $Re = 100$, $Pr = .7$, $N = 100$, $\tau = 2$, and $T_0/T_w = .1$. The steady-state solution is found by timestepping until a time independent solution is reached ($\Theta \approx .6745$). We then compare this numerical solution with a computation by a steady-state code implementing the algorithms in [15, 1].

We compute results for the following four cases:

- 1) $16 \times 16 \times 672$ level 0 grid, $\ell_{max} = 0$
- 2) $8 \times 8 \times 336$ level 0 grid, $\ell_{max} = 1$, $r_0 = 2$
- 3) $4 \times 8 \times 168$ level 0 grid, $\ell_{max} = 1$, $r_0 = 4$
- 4) $4 \times 4 \times 168$ level 0 grid, $\ell_{max} = 2$, $r_0 = 2$, $r_1 = 2$

The refinement strategy in cases 2–4 is to tag all cells for which $x/L < .07143$. Fig. 4 compares the computed results at steady-state ($\Theta = .6745$) for case 4 with results computed by the steady-state code described in [15, 1]; the bulk temperature profiles for the other three cases are indistinguishable from the case 4 curve. The results computed using the algorithm described here and the steady-state code agree fairly well.

We now present timings for these four cases. The calculations were all run on a single 300 Mhz processor of a DEC Alpha workstation to a final time of $\Theta = .6745$. The average percentage of the domain refined to the finest level is $7 \pm 1\%$ for cases 2-4. Table 3 shows the same fields shown in table 1. The results in table 3 again show a reduction in computational cost when adaptive mesh refinement is used. Case 4 shows the best reduction in computational cost over the uniform grid calculation. As in the case of the simultaneously developing pipe flow example, the comparative advantage of case 4 is probably due to the use of a refinement ratio of 4. However, the reduction in cost from using $r = 4$ is not as

great in three dimensions as it is in two.

Conservation Test: Shearing Flow in a Box

In this example we consider an idealized flow in a closed unit box with reflecting walls ($\epsilon = 0$, $\rho = 1$), to confirm that the algorithm conserves energy even when the grid structure is complex and changes with time, scattering is present, and the absorption coefficient is nonuniform. The initial velocities are

$$u = -\sin^2(\pi x) \sin(2\pi y)$$

$$v = \sin^2(\pi y) \sin(2\pi x)$$

with slip-wall boundary conditions. The walls are adiabatic. Viscosity and conduction are set to 0, while ρ and c_p are constant. Temperature is initialized to T_0 except for a hot region of temperature $8/3T_0$, centered at $(0.75, 0.25)$ and with radius 0.1.

The absorption coefficient κ is κ_0 throughout the domain, except for a disk of radius 0.1 at the center of the box where $\kappa = 50\kappa_0$. The base grid is 32×32 , with two levels of refinement by factors of 2 and 4. The grid is refined either where $\kappa = 50\kappa_0$ or where a marker for the fluid in the initial hot region is present. Figure 5 shows the temperature field at timesteps 0, 10 and 100 with no scattering, and at timestep 10 with a uniform scattering coefficient $\sigma = 10\kappa_0$. The main effect of scattering is the elimination of ray effects present in the results for absorption only.

As there is no heat transfer through the walls, the integral of enthalpy over the domain should be constant in time. In the experiment this quantity remained constant to 8 decimal places, with or without scattering. This precision is slightly better than expected, since

the relative tolerance required for convergence of the radiation solutions was 10^{-7} , and the ordinates were taken from a table with only 7 decimal places.

Flickering Laminar Methane-Air Diffusion Flame

Accounting for radiative heat transfer in the modeling of laminar flames has been shown to be important [19, 20, 21]. In this last example we combine our adaptive combined-mode heat transfer algorithm with an adaptive algorithm for unsteady low-Mach combustion [13] to perform an axisymmetric computation of a flickering, unconfined methane-air diffusion flame. The computation models the coannular burner used by Smyth *et al.* [22] in a experimental flame study. They report results that include the effect of acoustic forcing [22] and those that do not [23]. The latter case is the one computed here. Yam *et al.* [24] have also simulated this flow using a single grid projection method.

The burner consists of a fuel inlet with a radius of .55 cm surrounded by an annulus of coflowing air with an outer radius of 5.1 cm. The velocity of both inlet streams is 7.9 cm/sec. The flow develops as follows. Initially, the flame grows in length and oscillates in a non-periodic manner. After a short time, the flame reaches a “steady-state” in which it exhibits a periodic oscillatory behavior best described as flickering. The flame oscillations are caused by a buoyancy-induced Kelvin-Helmholtz type of instability.

We simulate this flame using a low-Mach number model for combustion which accounts for compressibility. We consider the gas to be composed of three species (methane, air, and product) and use a one-step kinetics mechanism. Properties are governed by temperature correlations. We assume a unity Lewis number and use a Prandtl number of .75. We refer the reader to [13] for further details.

We consider five cases, one in which radiative heat transfer is not accounted for and four with radiative transfer using different models for radiative properties:

- 1) no radiative heat transfer
- 2) constant absorption coefficient, $\kappa = 1.0 \text{ m}^{-1}$
- 3) constant absorption coefficient, $\kappa = 1.5 \text{ m}^{-1}$
- 4) wide-band weighted-sum-of-grey-gases (WBW) model with three bands [25]
- 5) wide-band weighted-sum-of-grey-gases (WBW) model with four bands [25].

In cases 4 and 5, we assume that the combustion product contains 18% H_2O , 8.5% CO_2 , and .9% CO . We use a 16×64 level 0 grid to cover the domain $0 \leq r \leq 6.4 \text{ cm}$, $0 \leq z \leq 25.6 \text{ cm}$. There are three additional levels of refinement. The refinement ratio $r_\ell = 2$ for $\ell = 0, 1, 2$, so that the equivalent uniform grid is 128×512 . The inlet boundaries are refined to level 3, the region $T > 1800 \text{ K}$ is refined to level 2, and the region in which the magnitude of the vorticity exceeds 50 sec^{-1} is refined to level 1. We use a Courant number of .4. All the computed flames establish periodic flickering by $t = 1.5 \text{ sec}$.

For each computed flame, we find the maximum temperature and compute the flickering frequency and the time-averaged flame length by using the complete flickering cycles (measured peak length to peak length) between $t = 1.5 \text{ sec}$ and $t = 3.0 \text{ sec}$. These values are reported in table 4 for all five cases. A time history of the flame length for case 5 is shown in figure 6 and the temperature field for that case during a single flame oscillation is displayed in figure 7.

The values for cases 2–5 with radiation do not differ significantly with one another. They all exhibit a roughly 100 K decrease in peak flame temperature, a slight decrease in average flame length, and a slight increase in flickering frequency compared to case 1. The decrease

in flame temperature is consistent with results reported elsewhere [19, 20, 21]. The decrease in flame length and increase in flickering frequency can probably be attributed to a decrease in buoyancy. For comparison, Smyth *et al.* report a flickering frequency of $12 \pm .5$ Hz [23] and an average flame height of 7.9 cm. (The flame height they report is the axial location of the end of the soot burnout region, which is typically beyond the maximum temperature location we use to define flame length [26].) Smyth does not report flame temperatures; Yam *et al.* compute a maximum flame temperature of roughly 1950 K.

Table 5 reports the CPU time per cell per level timestep advance for radiation and the total memory usage for all five cases. As expected, the CPU time spent on radiation modeling is roughly proportional to the number of bands. However, the peak memory usage increases much less dramatically. This is due to fact that the only additional data structure required for each new band is a set of flux registers.

Conclusions

We have presented a conservative, adaptive mesh algorithm for unsteady, combined mode heat transfer. The algorithm couples a new scheme for the modeling of unsteady radiative transport on locally refined meshes with an adaptive projection method for incompressible flow. This radiative transport scheme is itself based on a discrete ordinates algorithm for instantaneous radiative heat transfer on locally refined meshes. The methodology also incorporates a predictor-corrector formulation for second-order temporal accuracy.

The algorithm has been implemented and validated in two and three dimensions. The examples presented here demonstrate that the adaptive algorithm can compute accurate,

energy conserving solutions while showing a significant reduction in CPU and memory usage over an uniform grid calculation. The results also show that the scheme is second-order accurate in time and space if a second-order discretization of the RTE is used.

We have presented results for laminar flows only. Hence, in future work, we will investigate the issues in computing turbulent flows with radiative transport using the method described here. We will also extend the incorporation of our methodology with an adaptive projection method for unsteady low-Mach number combustion [13]. Finally, we will further investigate the use of bounded, high-resolution differencing schemes [18] for the discrete-ordinates equations on locally refined meshes.

Acknowledgments

This work was performed at Lawrence Berkeley National Laboratory with support provided by the Applied Mathematical Sciences Program of the DOE Office of Mathematics, Information, and Computational Sciences under contract DE-AC03-76SF00098. Additional support at McDermott Technology was provided by the Applied Mathematical Sciences Program of the DOE Office of Mathematics, Information, and Computational Science under Subcontract No. 3643100.

The code which implements the algorithm described in this paper is derived from the IAMR code [9] and shares a large common code base with it. We would like to thank the members of CCSE at LBNL who contributed to the development of that code.

References

- [1] W. A. Fiveland and J. P. Jessee, A Mathematical Model for Pulverized Coal Combustion in Axisymmetric Geometries, ASME/EPRI Joint Power Conference Rept. RDTPA 94-44, Phoenix, AZ, 1994.
- [2] M. J. Berger and J. Oliger, Adaptive Mesh Refinement for Hyperbolic Partial Differential Equations, *J. Comput. Phys.*, vol. 53, pp. 484–512, 1984.
- [3] M. J. Berger and P. Colella, Local Adaptive Mesh Refinement for Shock Hydrodynamics, *J. Comput. Phys.*, vol. 82, pp. 64–84, 1989.
- [4] J. B. Bell, M. J. Berger, J. S. Saltzman, and M. Welcome, Three Dimensional Adaptive Mesh Refinement for Hyperbolic Conservation Laws, *SIAM J. Sci. Comp.*, vol. 15, no. 1, pp. 127–138, 1994.
- [5] B. G. Carlson and K. D. Lathrop, Transport Theory—The Method of Discrete Ordinates, in H. Greenspan and C. N. Kelber and D. Okrent (eds.), *Computing Methods in Reactor Physics*, pp. 171–266, Gordon and Breach, New York, 1968.
- [6] E. E. Lewis and W. F. Miller, Jr., *Computational Methods of Neutron Transport*, pp. 116–207, American Nuclear Society, La Grange Park, IL. 1993.
- [7] W. A. Fiveland, Discrete-Ordinates Solutions of the Radiative Transport Equation for Rectangular Enclosures, *J. Heat Transfer*, vol. 106, no. 4, pp. 699–706, 1984.

- [8] J. P. Jessee, W. A. Fiveland, L. H. Howell, P. Colella, and R. B. Pember, An Adaptive Mesh Refinement Algorithm for the Radiative Transport Equation, *J. Comput. Phys.*, vol. 139, pp. 380–398, 1998.
- [9] A. S. Almgren, J. B. Bell, P. Colella, L. H. Howell, and M. L. Welcome, A Conservative Adaptive Projection Method for the Variable Density Incompressible Navier-Stokes Equations, *J. Comput. Phys.*, vol. 142, pp. 1–46, 1998.
- [10] R. B. Pember, A. S. Almgren, W. Y. Crutchfield, L. H. Howell, J. B. Bell, P. Colella, and V. E. Beckner, An Embedded Boundary Method for the Modeling of Unsteady Combustion in an Industrial Gas-Fired Furnace, Western States Section of the Combustion Institute Rept. WSS/CI 95F-165, Stanford, CA, 1995.
- [11] P. Colella, Multidimensional Upwind Methods for Hyperbolic Conservation Laws, *J. Comput. Phys.*, vol. 87, pp. 171–200, 1990.
- [12] A. S. Almgren, J. B. Bell, and W. G. Szymczak, A Numerical Method for the Incompressible Navier-Stokes Equations Based on an Approximate Projection, *SIAM J. Sci. Comput.*, vol. 17, pp. 358–369, 1996.
- [13] R. B. Pember, L. H. Howell, J. B. Bell, P. Colella, W. Y. Crutchfield, J. P. Jessee, and W. A. Fiveland, An Adaptive Projection Method for Unsteady, Low-Mach Number Combustion, Lawrence Berkeley National Laboratory Rept. LBNL-41339, Berkeley, CA, 1998.

- [14] W. A. Fiveland and A. S. Jamaluddin, Three-Dimensional Spectral Radiative Heat Transfer Solutions by the Discrete-Ordinates Method, *J. Thermophys. Heat Trans.*, vol. 5, no. 3, pp. 315–339, 1991.
- [15] W. A. Fiveland, Three-Dimensional Radiative Heat-Transfer Solutions by the Discrete-Ordinates Method, *J. Thermophys. Heat Trans.*, vol. 2, no. 4, pp. 309–316, 1988.
- [16] B. E. Pearce and A. F. Emery, Heat Transfer by Thermal Radiation and Laminar Forced Convection to an Absorbing Fluid in the Entry Region of a Pipe, *J. Heat Transfer*, vol. 92, pp. 221–230, 1970.
- [17] A. Harten, High Resolution Schemes for Hyperbolic Conservation Laws, *J. Comput. Phys.*, vol. 49, pp. 357–393, 1983.
- [18] J. P. Jessee and W. A. Fiveland, Bounded, High-Resolution Differencing Schemes Applied to the Discrete Ordinates Method, *J. Thermophys. Heat Trans.*, vol. 11, pp. 540–548, 1997.
- [19] Y. Liu and B. Rogg, Prediction of Radiative Heat Transfer in Laminar Flames, *Combust. Sci. Tech.*, vol. 118, pp. 127–145, 1996.
- [20] M. Smooke, A. Ern, Tanoff, B. Valdati, R. Mohammed, D. Marran, and M. Long, Computational and Experimental Study of NO in an Axisymmetric Laminar Diffusion Flame, *Twenty-Sixth Symposium (International) on Combustion*, Naples, Italy, pp. 813–821. The Combustion Institute, Pittsburgh, PA, 1996.

- [21] B. Bennett and M. Smooke, Local Rectangular Refinement with Application to Fluid Flow Problems, Dept. of Mech. Eng. Rept. ME-101-97, Yale University, New Haven, CT, 1997.
- [22] K. Smyth, J. Harrington, E. Johnsson, and W. Pitts, Greatly Enhanced Soot Scattering in Flickering CH_4 /Air Diffusion Flames, *Combust. Flame*, vol. 95, pp. 229–239, 1993.
- [23] K. Smyth. Flickering Flames as Testing Grounds for Reliable Models of Gas Combustion, Project Advisor Group Meeting and 1994 Contractors Review of Combustion Chemistry Team and Turbulent Flame Burners Team Rept., GRI, Chicago, IL, 1994.
- [24] C. Yam, K. Marx, J.-Y. Chen, and C.-P. Chen, Numerical Study of Flickering Frequency and Emission Index of a Methane Diffusion Flame for Varying Gravitational Force, Western States Section of the Combustion Institute Rept. WSS/CI 95F-223, Stanford, CA, 1995.
- [25] M. K. Denison and W. A. Fiveland, A Hybrid Wide-Band Correlated-k Weighted-Sum-of-Gray-Gas Model for Radiative Transfer in Non-homogeneous Gas Mixtures, 1997 ASME National Heat Transfer Conference, Baltimore, MD, 1997.
- [26] Smyth, K.C., National Institute of Standards and Technology, private communication, 1997.

Gridding			CPU Time		% CPU Time for Radiation	Peak Memory Usage
Level 0 grid	ℓ_{max}	r	Total(s)	$\mu s/cell$		Mb
1) 64×512	0		16790.	282.	15.1	29
2) 32×256	1	2	10330.	490.	21.8	17
3) 16×128	2	2,2	7958.	480.	18.6	16
4) 16×128	1	4	4849.	322.	14.9	14
5) 8×64	2	2,4	5167.	359.	12.3	14
6) 4×32	2	4,4	4883.	338.	12.9	14

Table 1: Timings for uniform grid and refined grid calculations on a single processor of a 533 MHz DEC Alpha workstation for the simultaneously developing pipe flow example.

Θ	4×32	q	8×64	q	16×128
.06875	8.755×10^{-3}	2.11	2.031×10^{-3}	2.02	5.010×10^{-4}
.1375	4.466×10^{-3}	2.01	1.108×10^{-3}	2.07	2.643×10^{-4}
.275	3.598×10^{-3}	1.93	9.432×10^{-4}	2.05	2.274×10^{-4}
.55	3.912×10^{-3}	1.93	1.024×10^{-3}	2.06	2.458×10^{-4}

Table 2: Normalized L_1 errors and convergence rates for the simultaneously developing pipe flow example.

Gridding			CPU Time		% CPU Time for Radiation	Peak Memory Usage
Level 0 grid	ℓ_{max}	r	Total(s)	$\mu s/cell$		Mb
1) $16 \times 16 \times 672$	0		191500.	748.	44.1	144
2) $8 \times 8 \times 336$	1	2	53470.	1491.	55.3	36
3) $4 \times 4 \times 168$	2	2,2	23120.	1073.	51.5	22
4) $4 \times 4 \times 168$	1	4	18000.	857.	43.6	22

Table 3: Timings for uniform grid and refined grid calculations on a single processor of a 300 MHz DEC Alpha workstation for the simultaneously developing three-dimensional flow through a square duct example.

Radiative Properties	Flickering Frequency (sec^{-1})	Flame Length (cm)	Maximum Flame Temperature (K)
1) no radiation	11.97	6.57	2190
2) $\kappa = 1.0 \text{ m}^{-1}$	12.25	6.08	2074
3) $\kappa = 1.5 \text{ m}^{-1}$	12.36	5.97	2058
4) 3-band WBW	12.24	6.10	2057
5) 4-band WBW	12.06	6.28	2065

Table 4: Comparison of results for the flickering flame example.

Radiative Properties	CPU Time for Radiation ($\mu s/\text{cell}$)	Peak Memory Usage (Mb)
1) no radiation	—	13
2) $\kappa = 1.0 \text{ m}^{-1}$	192	14
3) $\kappa = 1.5 \text{ m}^{-1}$	196	14
4) 3-band WBW	575	14
5) 4-band WBW	796	15

Table 5: Timings on a single processor of a 533 MHz DEC Alpha workstation for the flickering flame example.

Figure captions

Figure 1. Comparison of computed bulk temperature for case 6 of the simultaneously developing pipe flow example with the Pearce-Emery solution.

Figure 2. Comparison of computed Nusselt numbers for cases 1, 4, 5, and 6 of the simultaneously developing pipe flow example with the Pearce-Emery solution.

Figure 3. Computed normalized temperature $(T-T_0)/(T_w-T_0)$ at $\Theta = .06875, .1375, .275$, and $.55$ for case 6 of the simultaneously developing pipe flow example. The boundaries of the level 1 and 2 grids are shown as thin lines.

Figure 4. Comparison of the bulk temperature for case 4 of the simultaneously developing three-dimensional flow through a square duct example with the solution from the steady-state code described in [15, 1].

Figure 5. Evolution of an off-center hot spot in a spinning flow in a box with a central absorbing region. In the first three frames there is no scattering. The last frame (bottom right) shows the same calculation with scattering at the same time as the upper right frame.

Figure 6. Axial position of the maximum temperature of the flickering flame along the centerline axis as a function of time for case 5.

Figure 7. Temperature field of flickering flame during a single flame oscillation for case 5. The boundaries of the level 1, 2, and 3 grids are shown as thin lines in the plots.

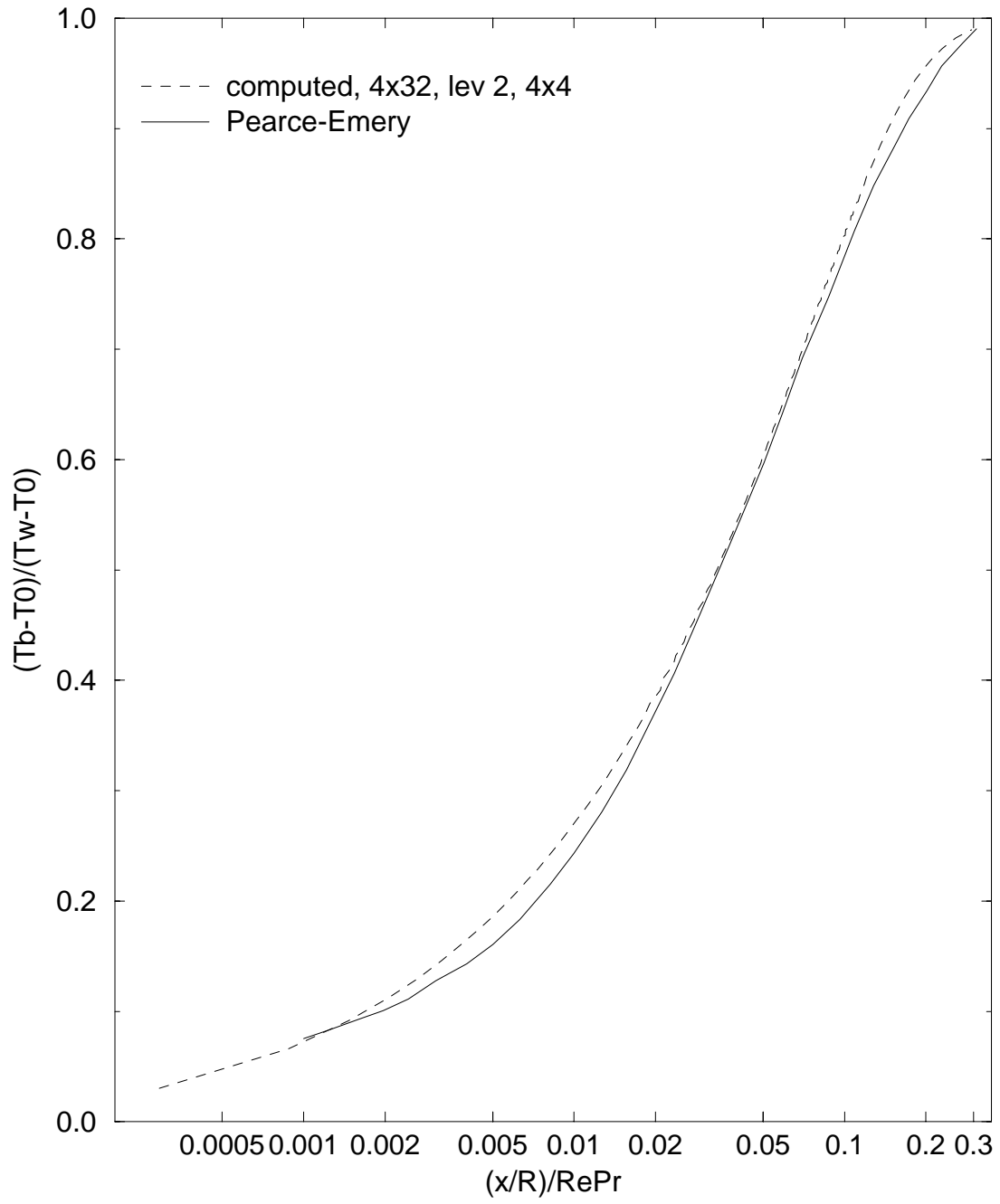


Figure 1: Comparison of the bulk temperature for case 6 of the simultaneously developing pipe flow example with the Pearce-Emery solution.

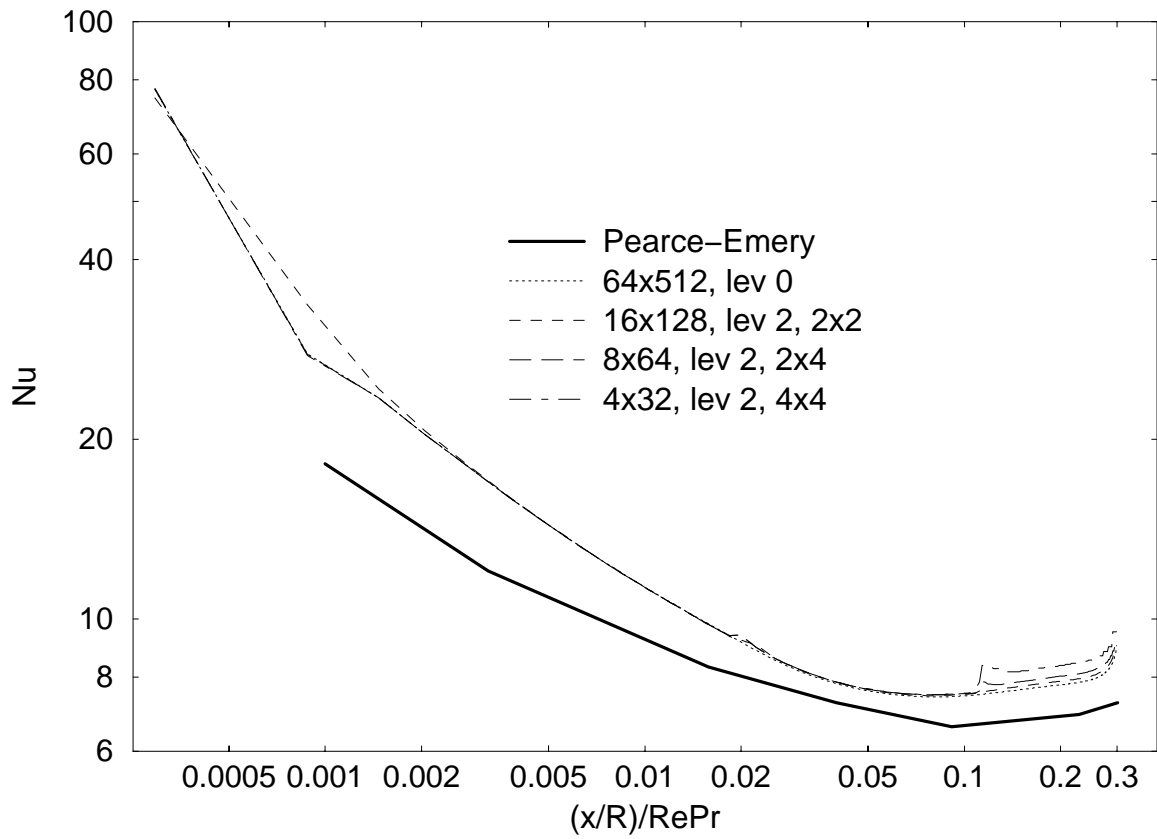


Figure 2: Comparison of the Nusselt number for cases 1, 4, 5, and 6 of the simultaneously developing pipe flow example with the Pearce-Emery solution.

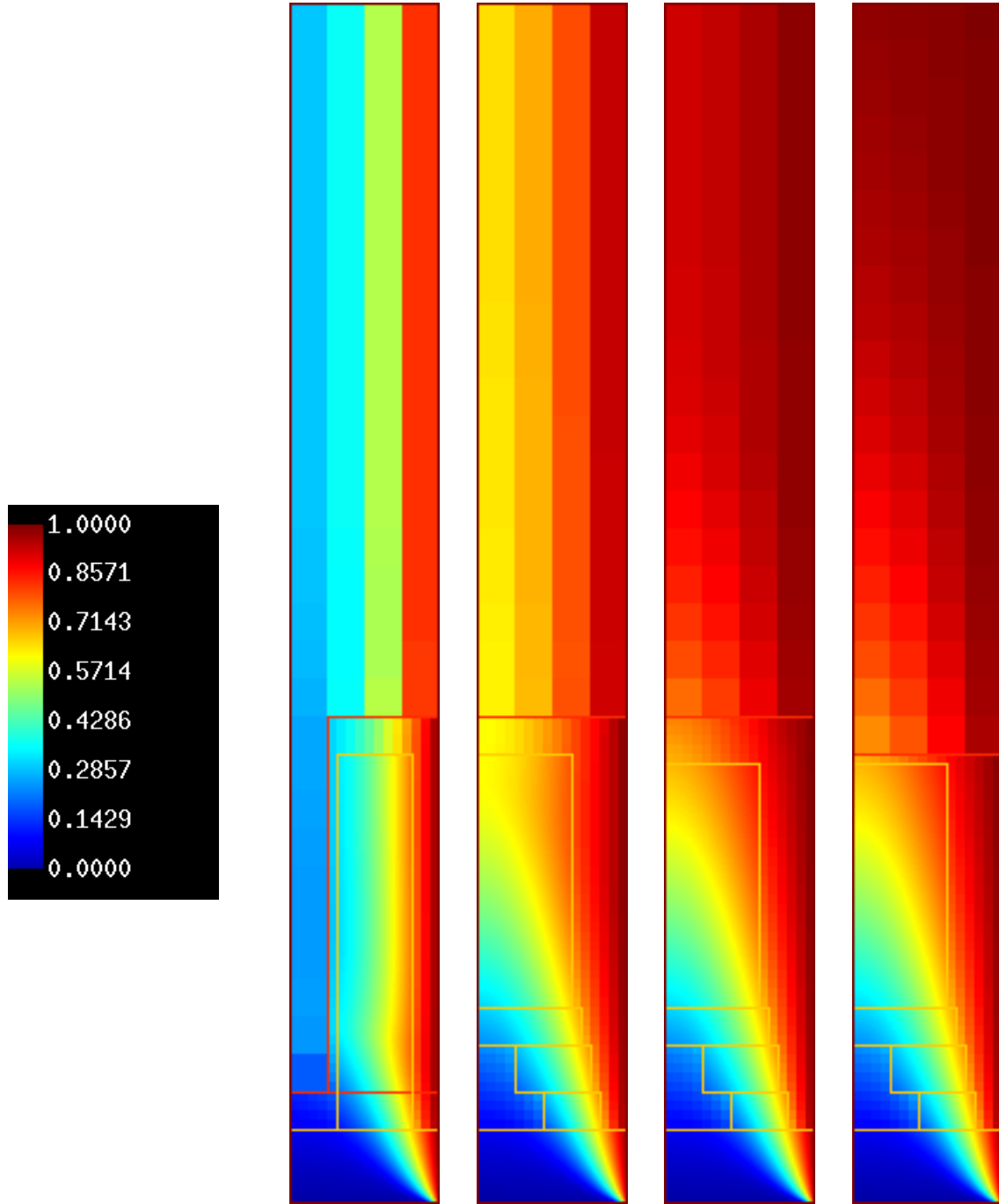


Figure 3: Computed normalized temperature $(T - T_0)/(T_w - T_0)$ at $\Theta = .06875, .1375, .275,$ and $.55$ for case 6 of the simultaneously developing pipe flow example. The boundaries of the level 1 and 2 grids are shown as thin lines.

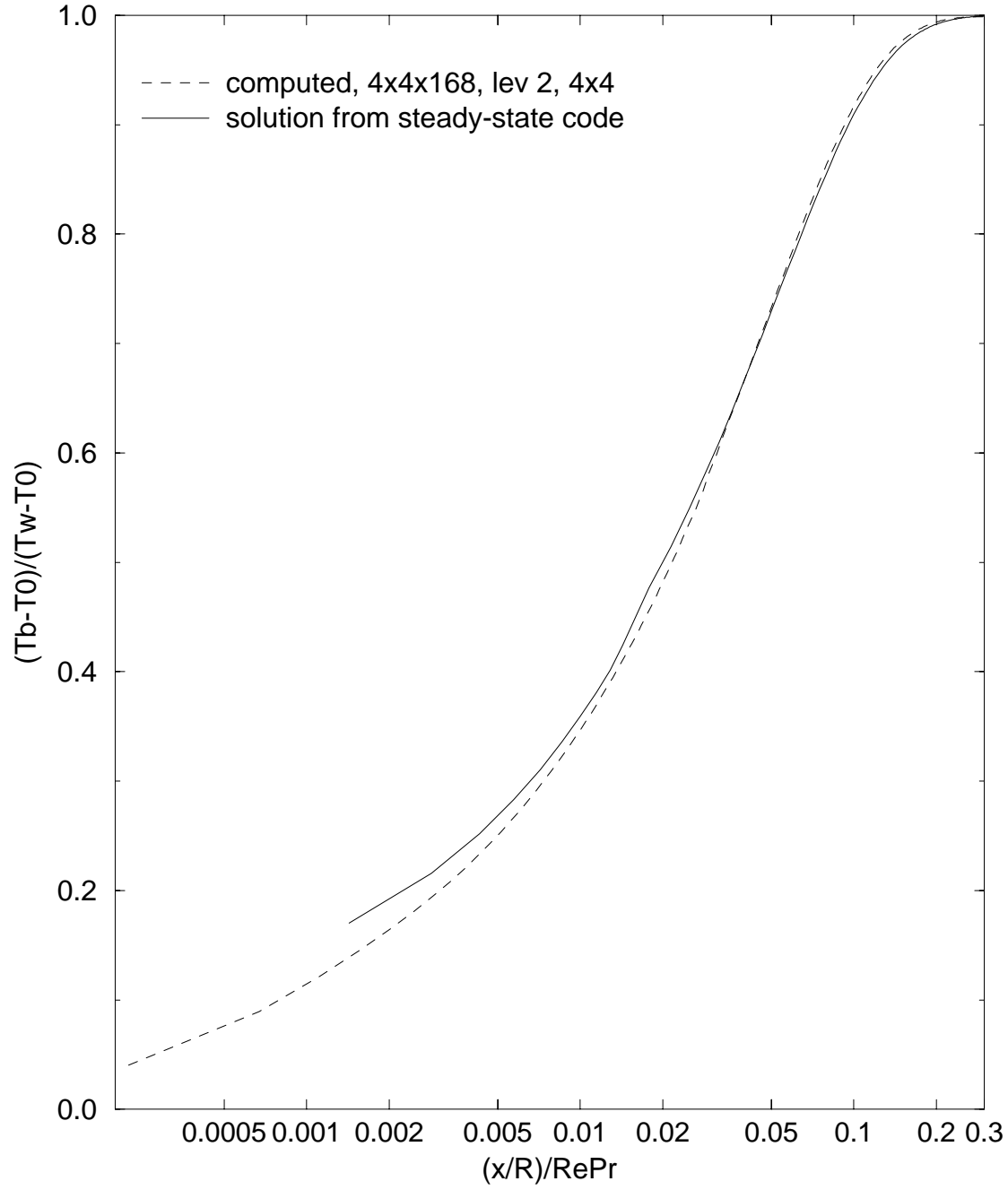


Figure 4: Comparison of the bulk temperature for case 4 of the simultaneously developing three-dimensional flow through a square duct example with the solution from the steady-state code described in [15, 1].

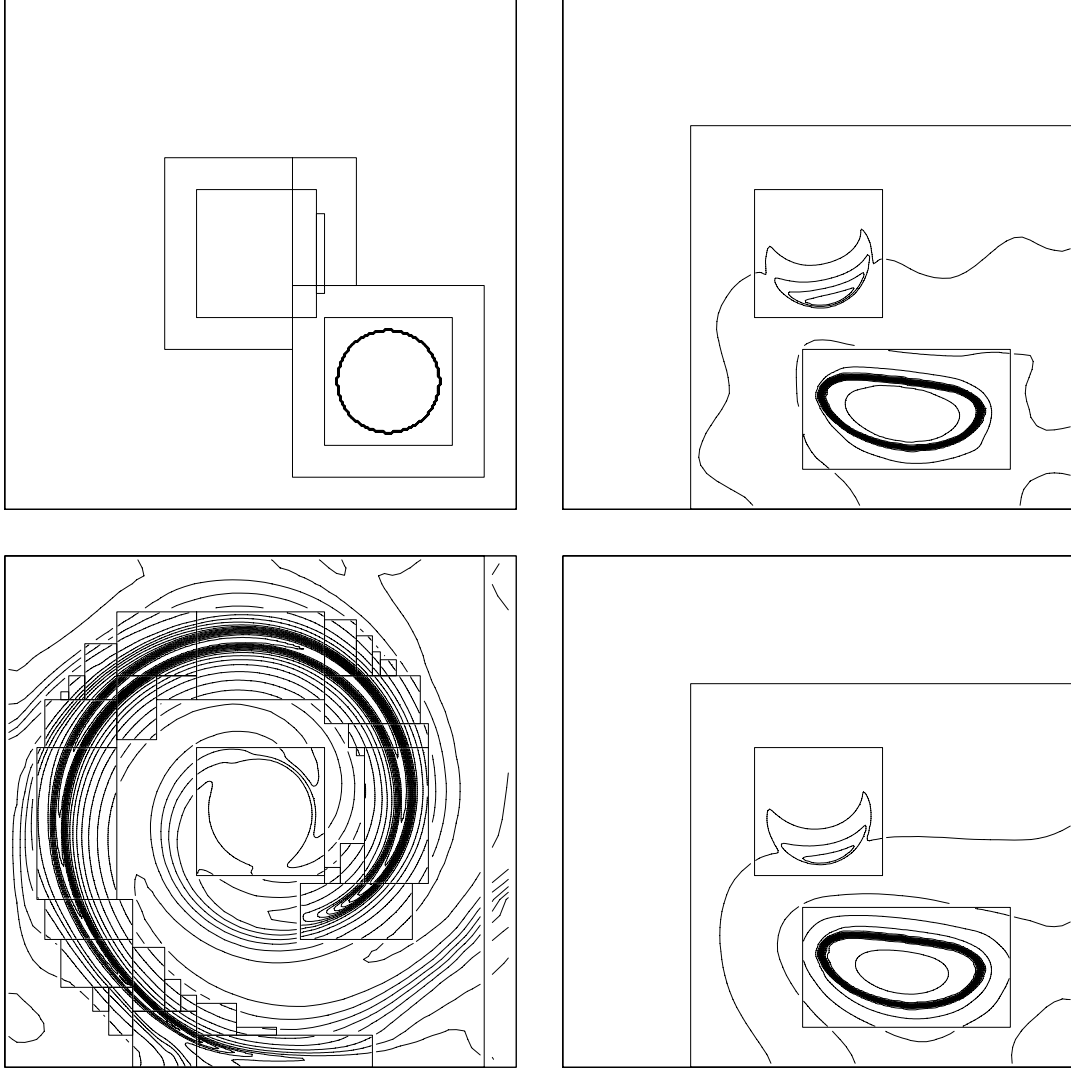


Figure 5: Evolution of an off-center hot spot in a spinning flow in a box with a central absorbing region. In the first three frames there is no scattering. The last frame (bottom right) shows the same calculation with scattering at the same time as the upper right frame.

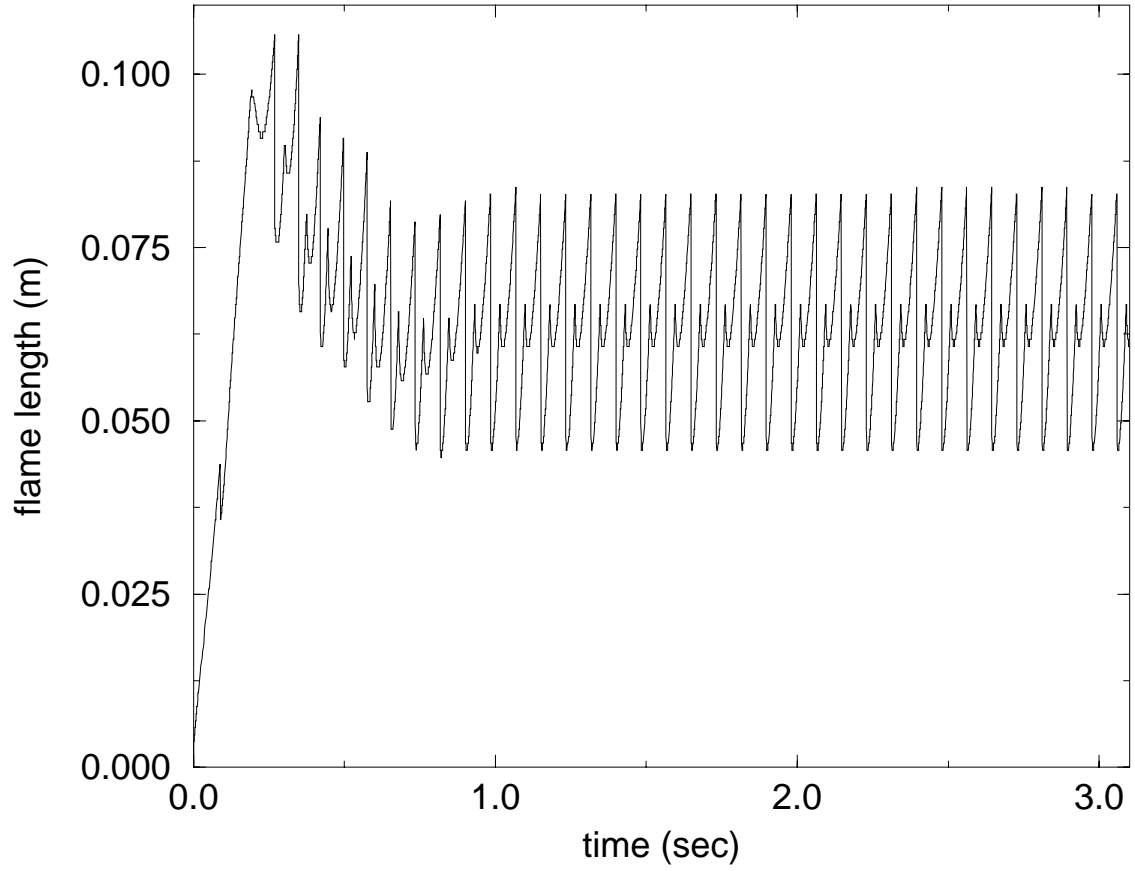


Figure 6: Axial position of the maximum temperature of the flickering flame along the centerline axis as a function of time for case 5.

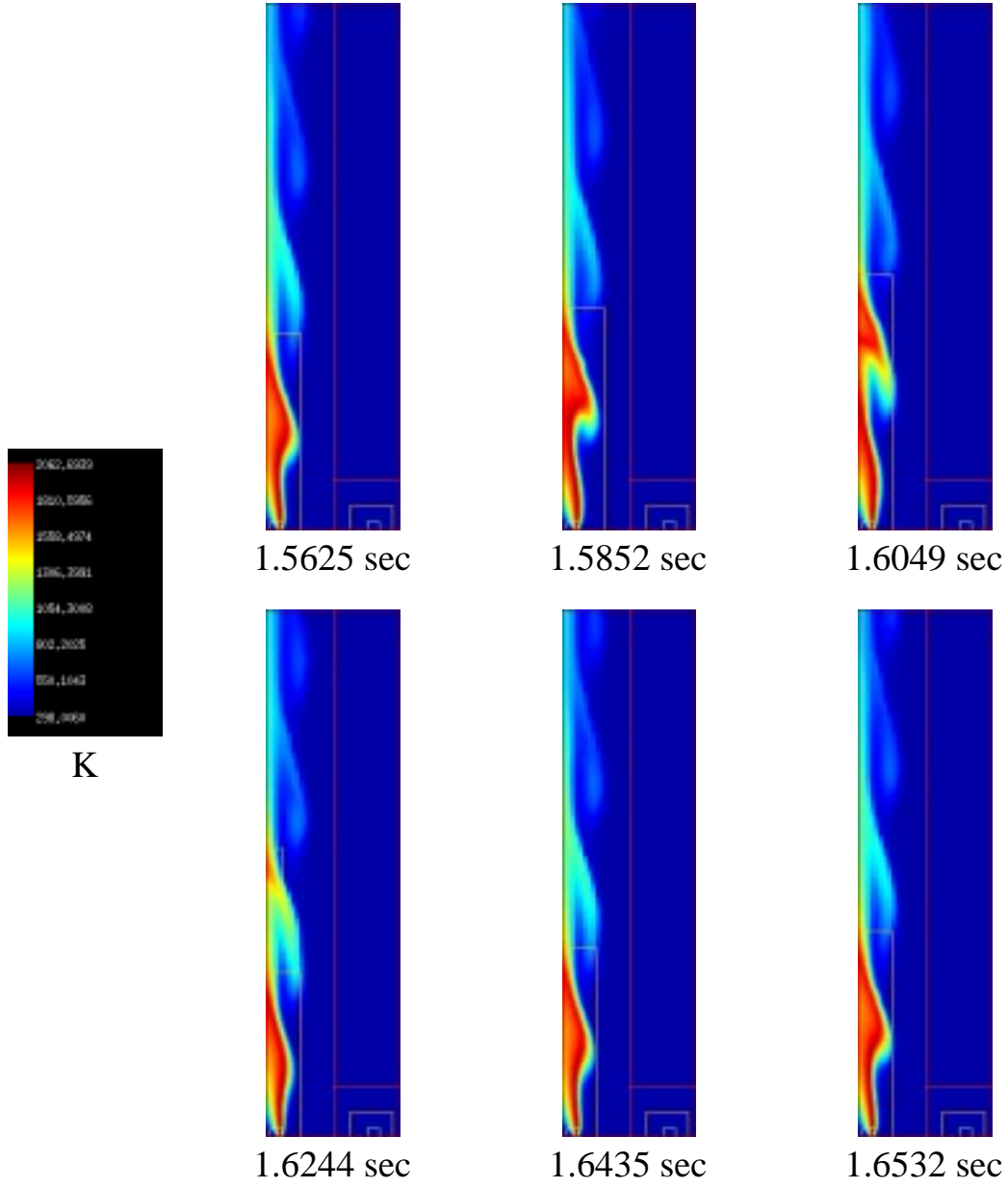


Figure 7: Temperature field of flickering flame during a single flame oscillation for case 5.

The boundaries of the level 1, 2, and 3 grids are shown as thin lines in the plots.